

1 **Tracking surface ozone responses to clean air actions under**
2 **a warming climate in China using machine learning**

3 Jie Fang¹, Yunjiang Zhang^{1*}, Didier Hauglustaine², Bo Zheng³, Ming Wang¹, Jingyi
4 Li¹, Yong Sun⁴, Haiwei Li¹, Junfeng Wang¹, Yun Wu¹, Bin Yuan⁵, Mindong Chen¹,
5 Xinlei Ge⁶

6 ¹Jiangsu Key Laboratory of Atmospheric Environment Monitoring and Pollution Control, School of
7 Environmental Science and Engineering, Nanjing University of Information Science and Technology,
8 Nanjing 210044, China

9 ²Laboratoire des Sciences du Climat et de l'Environnement, CNRS-CEA-UVSQ, Université Paris-Saclay,
10 Gif-sur-Yvette, France

11 ³Institute of Environment and Ecology, Tsinghua Shenzhen International Graduate School, Tsinghua
12 University, Shenzhen 518055, China

13 ⁴State Key Laboratory of Tibetan Plateau Earth System, Environment and Resources, Institute of Tibetan
14 Plateau Research, Chinese Academy of Sciences, Beijing 100101, China

15 ⁵College of Environment and Climate, Institute for Environmental and Climate Research, Guangdong-
16 Hongkong-Macau Joint Laboratory of Collaborative Innovation for Environmental Quality, Jinan
17 University, Guangzhou 511443, China

18 ⁶School of Energy and Environment, Southeast University, Nanjing 210096, China

19 *Correspondence to:* Yunjiang Zhang (yjzhang@nuist.edu.cn)

20

21 **Abstract.** Surface ozone, a major air pollutant with important implications for air quality,
22 ecosystems, and climate, shows long-term trends shaped by both anthropogenic and climatic drivers.
23 Here, we developed a machine learning-based approach, namely the fixed emission approximation
24 (FEA), to decouple the effects of meteorological variability and anthropogenic emissions on
25 summertime ozone trends in China under the clean air actions. Anthropogenic emissions drove an
26 approximately $+23.2 \pm 1.1 \mu\text{g m}^{-3}$ increase in summer maximum daily 8-hour average ozone during
27 2013–2017, followed by an approximately $-4.6 \pm 1.5 \mu\text{g m}^{-3}$ decrease between 2017 and 2020 in
28 response to strengthened emission controls. In contrast, meteorological anomalies, including
29 heatwaves and rainfall conditions, emerged as substantial drivers of ozone variability during 2020–
30 2023. Satellite-derived formaldehyde-to-nitrogen dioxide ratios revealed widespread urban volatile
31 organic compounds-limited regimes for ozone production, with a shift toward nitrogen oxides-
32 limited sensitivity under influence of heatwaves. Extending the FEA framework to assess long-term
33 climate influences from 1970 to 2023, we find that sustained climate warming has driven a
34 substantial increase in urban summertime ozone in China. These results demonstrate that climate
35 change was increasingly offsetting the benefits of emission reductions and highlight the need for
36 integrated ozone mitigation strategies that jointly address emission controls and climate adaptation
37 in a warming world.

38 **1 Introduction**

39 Surface ozone (O_3) is a critical air pollutant that poses significant threats to human health (Knowlton et
40 al., 2004), ecosystems (Agathokleous et al., 2020), and climate (Fishman et al., 1979; Hauglustaine et
41 al., 1994). It forms through complex photochemical reactions involving nitrogen oxides (NO_x) and
42 volatile organic compounds (VOCs) in the presence of sunlight (Jacob, 2000; Wang et al., 2017),
43 exhibiting a nonlinear response to its precursors (Guo et al., 2023; Liu and Shi, 2021; Wang et al., 2023a).
44 Controlling ozone pollution remains a global environmental challenge. In recent years, China has
45 implemented a series of national clean air actions, most notably the Air Pollution Prevention and Control
46 Action Plan (2013–2017) and the Three-Year Action Plan for Winning the Blue-Sky War (2018–2020)
47 (Geng et al., 2024; Zhang et al., 2019; Zheng et al., 2018), that have markedly improved air quality,
48 particularly by reducing fine particulate matter ($PM_{2.5}$) (Geng et al., 2024; Zhang et al., 2019). However,
49 surface ozone levels have continued to rise in many regions, raising concerns over the complex drivers
50 of ozone trends and highlighting the need for scientific attribution to guide effective mitigation strategies
51 (Li et al., 2019a; Liu et al., 2023; Wang et al., 2023a; Weng et al., 2022).

52 Long-term ozone variability is jointly influenced by anthropogenic emissions and weather
53 conditions as well as regional climate (Hallquist et al., 2016; Li et al., 2019b; Wang et al., 2022a). While
54 emission controls directly regulate precursor abundance, climate change modulates ozone through
55 chemical feedbacks, meteorological dynamics, and biosphere–atmosphere interactions (Ma and Yin,
56 2021; Xue et al., 2020). Over the past century, global surface temperatures have substantially increased
57 relative to the pre-industrial baseline (1850–1900), driven largely by human activities (IPCC, 2021). In
58 such a warming world, extreme climate anomalies – such as heatwaves and persistent rainfall shifts –
59 were expected to be intensified (Li et al., 2025a; Li et al., 2025b). These events were increasingly
60 recognized as critical modulators of ozone variability through their impacts on photochemistry and
61 precursor emissions (Gao et al., 2023; Pu et al., 2017; Wang et al., 2022a).

62 Quantifying the respective roles of anthropogenic emissions and meteorological variability in
63 driving ozone trends is therefore essential for evaluating the effectiveness of clean air policies (Li et al.,
64 2019a; Liu et al., 2023). Previous studies have reported rapid increases in surface ozone concentrations

65 in urban cluster regions in China – such as the Beijing–Tianjin–Hebei (BTH) and Yangtze River Delta
66 (YRD) – during the Phase I (2013 – 2017), with increases of approximately 28% and 18%, respectively
67 (Chen et al., 2020; Li et al., 2019a; Liu et al., 2023). In contrast, a modest decline in ozone levels was
68 observed during 2018 – 2020, largely attributed to emission reductions (Li et al., 2021; Liu and Wang,
69 2020b; Wang et al., 2024b; Wang et al., 2023a). However, since 2021, observations indicate a renewed
70 increase in ozone concentrations (Fig. S1). These fluctuations suggest oscillating trends over the past
71 decade, the drivers of which remain poorly constrained.

72 Two main approaches have been applied to attribute air pollution trends: chemical transport models
73 (CTMs) (Li et al., 2021; Liu et al., 2023; Liu and Wang, 2020a) and data-driven statistical frameworks
74 (Li et al., 2019a; Li et al., 2019b; Li et al., 2020). The CTMs simulate atmospheric composition based
75 on emission inventories, meteorological fields, and chemical mechanisms (Ivatt et al., 2022; Liu and Shi,
76 2021; Liu et al., 2023; Ye et al., 2024). They allow attribution of trend components to emissions or
77 meteorology, and can also resolve sector-specific impacts. However, these models face challenges,
78 including uncertainties and temporal lags in emission inventories. Statistical models, on the other hand,
79 rely on observational datasets and predictor-response relationships without requiring explicit emissions
80 or chemical schemes (Li et al., 2019a; Li et al., 2019b; Li et al., 2020; Zhai et al., 2019). With the growing
81 availability of atmospheric big data, machine learning models have emerged as useful tools for trend
82 attribution (Dai et al., 2023; Grange et al., 2018; Vu et al., 2019; Zhang et al., 2025; Zheng et al., 2023).
83 For instance, Grange et al. (2018) developed a random forest-based framework to isolate meteorological
84 influences on particulate matter. Similarly, Wang et al. (2023) used an enhanced extreme gradient
85 boosting (XGBoost) model to analyze spatial and temporal ozone patterns in China from 2010 to 2021,
86 confirming that emission reductions played a key role in recent declines. Other recent efforts have
87 extended statistical models to long-term assessments of air pollution drivers under climate change (Wang
88 et al., 2022b).

89 Here, we developed a machine learning-based model framework – fixed emission approximation
90 (FEA) – to quantify the relative contribution of anthropogenic emissions and meteorological conditions
91 in shaping summertime surface ozone trends in China. Applying the FEA to nationwide observational
92 data from 2013 to 2023, we identified three phases of ozone evolution corresponding to the major clean
93 air actions. We further analyzed short-term ozone anomalies associated with extreme weather events,

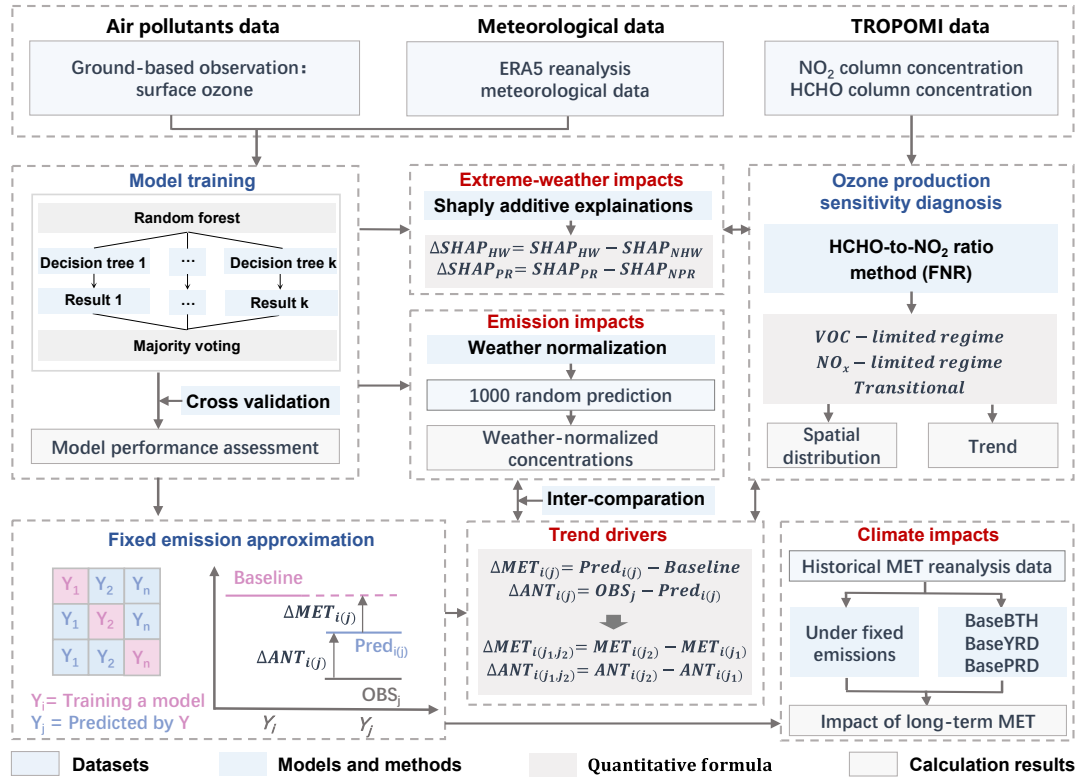
94 such as the 2022 heatwave and seasonal rainfall. To characterize ozone production regimes, we integrated
95 satellite-derived formaldehyde-to-nitrogen dioxide (HCHO/NO₂, FNR) ratios from the tropospheric
96 monitoring instrument (TROPOMI), revealing spatiotemporal shifts in ozone formation sensitivity
97 across China. Finally, we extend our FEA analysis to evaluate climate-driven ozone trends from 1970 to
98 2023, using historical meteorological reanalysis data. Collectively, these analyses provide an integrated
99 understanding of how anthropogenic and climatic factors jointly shape surface ozone dynamics under a
100 warming climate.

101 **2 Data and methods**

102 **2.1 Data sources and methodology overview**

103 Figure 1 provides an overview of the data analysis and methodological framework employed in this
104 study. We first integrated multi-dimensional datasets, including hourly surface air pollutant
105 concentrations, meteorological reanalysis fields, and satellite remote sensing data. Hourly surface
106 observations of ozone, NO₂, carbon monoxide (CO), and PM_{2.5} were accessed from the National
107 Environmental Monitoring Center of China through the open website <https://air.cnemc.cn:18007/> (last
108 accessed: May 20, 2024). Hourly meteorological data with a spatial resolution of 0.25° × 0.25° were
109 sourced from the ERA5 reanalysis dataset provided by the European Centre for Medium-Range Weather
110 Forecasts (ECMWF) and are available for download at <https://cds.climate.copernicus.eu> (last accessed:
111 March 20, 2025). Detailed variables are listed in Table S1. The time variables – hour (hour of day) and
112 month (month of year) – are used as emission surrogates to capture regular diurnal and seasonal
113 variations in anthropogenic activity. A similar strategy is widely applied in previous studies about long-
114 term trends in air pollutants (e.g., Grange et al., 2018; Vu et al., 2019) to separate short-term cyclical
115 emission variability from long-term trends. For 2013 – 2014, the surface MDA8 ozone data were
116 obtained from the Tracking Air Pollution in China (TAP) dataset (Geng et al., 2021), which can be
117 downloaded from <http://tapdata.org> (last accessed: May 20, 2024). The TROPOMI on the Sentinel-5P
118 satellite provides global continuous observation data for two indicators of ozone precursors: NO₂ and
119 HCHO column concentrations (Lamsal et al., 2014; Shen et al., 2019). The FNR was used as a proxy for
120 VOC/NO_x reactivity and as a diagnostic indicator of ozone formation sensitivity (Sillman, 1995), to

121 explain and verify the impact of extreme weather and anthropogenic emissions on ozone. Details of the
 122 ozone sensitivity diagnostic method are provided in Text S1.



140 emission patterns (e.g., diurnal cycles), thereby enabling the model to isolate the long-term emission-
141 driven component of ozone changes (Grange et al., 2018; Meng et al., 2025; Shi et al., 2021; Vu et al.,
142 2019). The meteorological parameters include 18 distinct variables at different altitudes (see Table S1).
143 It should be noteworthy that surface air pollutant observations for each city represent multi-site averages
144 rather than data from a single monitoring station, which reduces the influence of local representativeness
145 uncertainty. The meteorological data are obtained from the nearest grid cell corresponding to each city,
146 ensuring spatial consistency between the pollutant and meteorological datasets. This approach was
147 similar to the methodologies widely adopted in previous studies (Shi et al., 2021; Wang et al., 2025; Yao
148 et al., 2024; Zheng et al., 2023). Our modeling strategy involves building and predicting models for
149 individual cities and for each year from 2015 to 2023, which helps in minimizing the uncertainty caused
150 by surface heterogeneity. Due to the lack of available observational data for many cities in 2013 and
151 2014, we did not develop models for these two years. In our approach, 80% of the dataset is used for
152 model training, while the remaining 20% is reserved for testing. We perform ten-fold cross-validation
153 and assess model performance using seven statistical metrics, as listed in Table S2.

154 Following the construction of the machine learning models for individual cities and years, we
155 introduce the FEA approach. The key principle of FEA is the assumption that the total emissions of ozone
156 precursors remain unchanged from the baseline year. Specifically, we establish hourly-resolution models
157 for the baseline year (i) during the summer season (June to August) as a reference for anthropogenic
158 emissions, represented by the pink solid line in Fig. 1. These models are then applied to predict ozone
159 concentrations under the meteorological conditions of the prediction year (j), while holding the emission
160 levels constant at those of the baseline year (i), as shown by the blue solid line in Fig. 1. The difference
161 between the predicted values ($Pred_i$) and the observed values (OBS_i) for the baseline year (i) represents
162 the model residuals (RES_i), as shown in Eq. (1). The difference in observed MDA8 ozone concentrations
163 between baseline year i and prediction year j is driven by the differences in meteorological conditions
164 ($MET_{i(j)}$) and anthropogenic emission controls ($ANT_{i(j)}$) (Eq. 2). The prediction result $Pred_{i(j)}$ obtained
165 by applying the model trained with data from year i to the meteorological conditions of year j , the
166 difference between $Pred_{i(j)}$ and Baseline ($Pred_i$) is driven by $MET_{i(j)}$, while the difference between
167 $Pred_{i(j)}$ and the observed levels in year j (OBS_j), minus the RES_i , yields the ozone variation driven by
168 ($ANT_{i(j)}$). Therefore, $MET_{i(j)}$ and $ANT_{i(j)}$ can be quantified and calculated using Eqs. (3-4).

169 $OBS_i = Pred_i + RES_i ,$ (1)

170 $OBS_{i(j)} = MET_{i(j)} + ANT_{i(j)} ,$ (2)

171 $MET_{i(j)} = Pred_{i(j)} - Pred_i ,$ (3)

172 $ANT_{i(j)} = OBS_j - Pred_{i(j)} - RES_i ,$ (4)

173 The difference in observed MDA8 ozone concentrations between two different prediction years (j_1 ,
 174 j_2) is driven by the differences in meteorological conditions ($\Delta MET_{i(j1,j2)}$) and anthropogenic emission
 175 controls ($\Delta ANT_{i(j1,j2)}$) (Eq. 5). The term $\Delta MET_{i(j1,j2)}$ represents the changes in meteorological
 176 conditions and can be calculated by the difference between the predicted values, $Pred_{i(j1)}$ and
 177 $Pred_{i(j2)}$, for the corresponding years (Eq. 6). Similarly, the value of $\Delta ANT_{i(j1,j2)}$, representing the
 178 change in anthropogenic emissions between the two years j_1 and j_2 , can be therefore calculated using Eq.
 179 (7). By performing these calculations, we can isolate and quantify the contributions of meteorological
 180 conditions and anthropogenic emission controls to the observed ozone trends. We used a cross-matrix
 181 research method to assess the uncertainty of FEA, with specific formulas available in Supporting Method
 182 S2.

183 $\Delta OBS_{(j1,j2)} = \Delta MET_{i(j1,j2)} + \Delta ANT_{i(j1,j2)} ,$ (5)

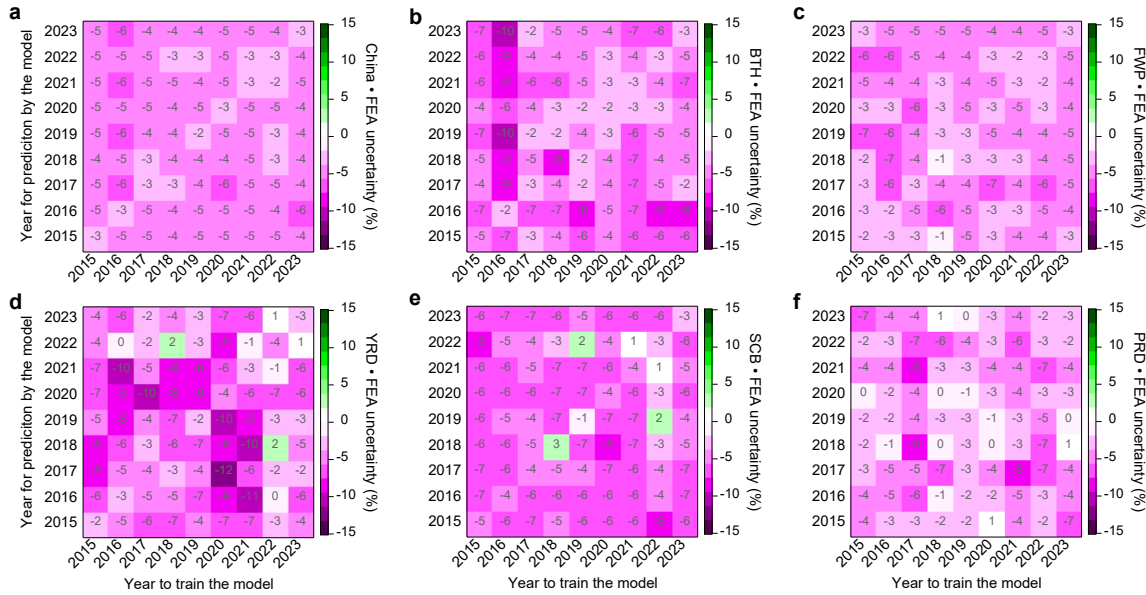
184 $\Delta MET_{i(j1,j2)} = Pred_{i(j2)} - Pred_{i(j1)} ,$ (6)

185 $\Delta ANT_{i(j1,j2)} = ANT_{i(j2)} - ANT_{i(j1)} = (OBS_{j2} - Pred_{i(j2)} - RES_i) - (OBS_{j1} - Pred_{i(j1)} - RES_i)$

186 $= (OBS_{j2} - OBS_{j1}) - (Pred_{i(j2)} - Pred_{i(j1)}) ,$ (7)

187 Model performance was first evaluated through ten-fold cross-validation, revealing high predictive
 188 skill between observed and predicted MDA8 ozone levels during 2015-2023 in the BTH regions (Fig.
 189 S2). The index of agreement (IOA) ranged from 0.96 to 0.97, with correlation coefficients (R) between
 190 0.93 and 0.95. Root mean square errors (RMSE) and normalized mean bias (NMB) varied from 16.9 to
 191 $21.9 \mu\text{g m}^{-3}$ and 8 to 25%, respectively, indicating high model accuracy. Nationally, the model yielded R
 192 values of 0.88–0.91 and IOA of 0.93–0.95, with errors remaining within acceptable ranges (Tables S3–
 193 S8). To assess uncertainty stemming from interannual model training variability, we applied a matrix-
 194 based resampling approach (see Text S2). As shown in Fig. 2, the relative difference in residuals ranged
 195 from -9% to 3%, and remained within $\pm 12\%$ for all regions – supporting the robustness of the FEA

196 method. Notably, inclusion of time-related variables could reduce model uncertainty compared to
 197 simulations excluding these predictors. The average uncertainty decreased by approximately 2–4% at the
 198 regional-mean level (Fig. S3).



199
 200 **Figure 2. Uncertainty assessment of the FEA method.** The uncertainty for the FEA method is calculated using the
 201 approach described in Text S2. The x-axis represents the years used for model training, and the y-axis represents the
 202 years predicted by the trained model. The diagonal line in each sub-panel represents the changes in the residuals of
 203 the models.

204 **2.3 Weather normalization analysis**

205 To compare the FEA method with other commonly used statistical approaches, we also applied the
 206 widely adopted meteorological normalization technique based on the RF algorithm (Grange et al., 2018;
 207 Vu et al., 2019). This approach constructs a regression model that relates air pollutant concentrations to
 208 meteorological parameters and emission surrogate indicators (i.e., time variables such as unix time, day
 209 of year, day of month, and hour of day) (Grange et al., 2018; Vu et al., 2019). Once the model is trained,
 210 air pollutant concentrations are predicted by randomly resampling meteorological variables from long-
 211 term historical meteorological datasets, thereby generating a new ensemble of predictions (Vu et al.,
 212 2019). These predictions are made under consistent meteorological conditions, enabling the isolation of
 213 meteorological influences from anthropogenic emission effects on air pollutant trends. The resulting
 214 weather-normalized pollutant concentrations (Fig. 1) represent the levels expected under average
 215 meteorological conditions, thus reflecting the impact of emission changes alone. In this study, the
 216 meteorological normalization follows this established framework, with meteorological variables

217 randomly sampled from the long-term dataset spanning 1970-2023. Each normalization process involves
218 1,000 iterations, and the arithmetic mean of these iterations' simulated values was adopted as the final
219 normalized result. The alignment between FEA-based and weather-normalized trends (Fig. S4) affirms
220 the robustness of the FEA framework.

221 **2.3 Quantification of extreme weather-driven changes in ozone**

222 An unprecedented and persistent heatwave struck central and eastern China during the summer of
223 2022, with the YRD experiencing the most severe impacts (Wang et al., 2023b; Zhang et al., 2023). This
224 event has been identified as the longest-lasting and most intense heatwave since at least 1961 (Mallapaty,
225 2022). In contrast, the Yangtze-Huaihe region is climatologically prone to sustained extreme precipitation,
226 where prolonged rainfall episodes frequently occur during the East Asian summer monsoon (Yin et al.,
227 2020). Together, the extreme heatwave (HW) in 2022 and recurrent prolonged rainfall (PR) events
228 provide unique and physically realistic atmospheric conditions to investigate the impacts of typical
229 weather extremes on surface ozone.

230 To quantify the contributions of extreme meteorological conditions to ozone variability, we applied
231 the SHapley Additive exPlanations (SHAP) method (Lundberg et al., 2020) to interpret predictions from
232 the random forest model. SHAP assigns an importance value to each input feature k , representing its
233 marginal contribution to the model-predicted MDA8 ozone. The PR period was defined as 15 June to 15
234 July for each year, while the remaining period from June to August was classified as the non-prolonged
235 rainfall (NPR) period. The HW event in 2022 was defined as 16 July to 31 August, with the same calendar
236 period in other years designated as non-heatwave (NHW) conditions.

237 SHAP values were calculated for all input features during the PR and NPR periods, as well as during
238 the HW and NHW periods, respectively. The relative changes in SHAP values ($\Delta SHAP$) between these
239 conditions were used to assess the responses of MDA8 ozone to the rainy season or the 2022 heatwave
240 weather conditions, as per the following Eqs:

$$241 \Delta SHAP_k = SHAP_{PR} - SHAP_{NPR} \quad (8)$$

$$242 \Delta SHAP_k = SHAP_{HW} - SHAP_{NHW} \quad (9)$$

243 **2.5 FEA-based assessment of climate change impacts on ozone**

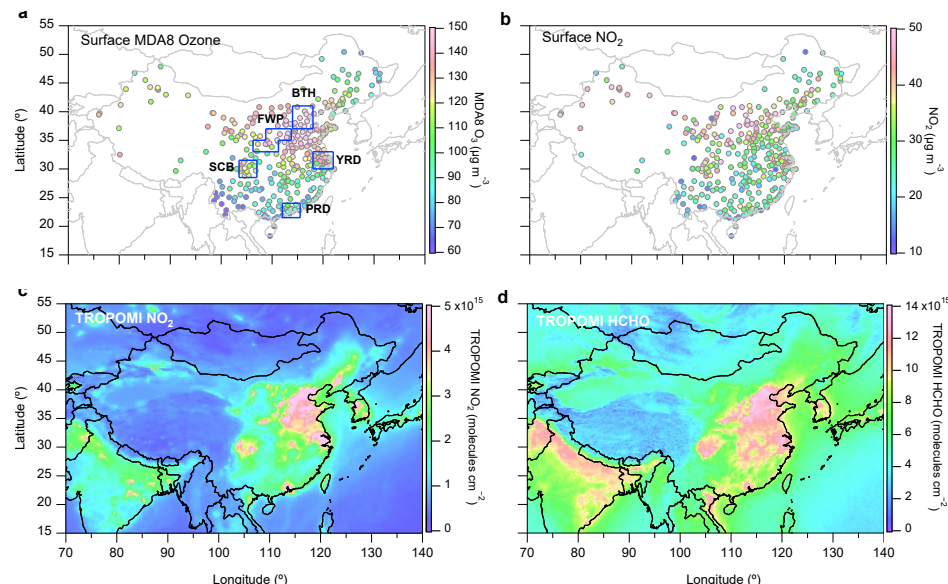
244 To evaluate the long-term impact of climate change on surface ozone concentrations across

245 China from 1970 to 2023, we extended the framework of our machine learning-based FEA method.
246 The core idea of this analysis is to isolate the influence of long-term meteorological variability on
247 ozone while assuming fixed anthropogenic emissions. Given the availability of relatively complete
248 and continuous hourly ozone observations and meteorological data from 2015 to 2023, this period
249 was used to construct nine emission baseline scenarios. Following the modeling protocol described in
250 Section 2.2, nine independent random forest models were trained for each city and scenario, with each
251 year from 2015 to 2023 serving as an emissions reference. Model inputs included hourly ozone
252 observations, key meteorological predictors, and time-related variables (hour of day and month of year).
253 The trained models were then applied to historical meteorological reanalysis data from 1970 to 2023 to
254 simulate ozone trends under fixed emissions (Fig. 1), yielding nine independent ozone trajectories, each
255 reflecting the influence of long-term meteorological variability under a different fixed-emissions
256 assumption. While the choice of emission baseline may affect the absolute magnitude of simulated ozone,
257 it does not alter the primary objective: assessing the sensitivity of surface ozone to meteorological drivers
258 over multidecadal timescales (Lecœur et al., 2014; Leung et al., 2018; Wang et al., 2022b). This approach
259 could capture the climate-induced ozone signal while adopting the common assumption that emissions
260 are not themselves influenced by climate change – a simplification consistent with prior attribution
261 studies (Dang and Liao, 2019; Leung et al., 2018; Shen et al., 2017; Wang et al., 2022b). For comparison,
262 we also estimated the impact of anthropogenic emission changes on ozone concentrations during 2015–
263 2023 using the same FEA methodology and the complete hourly dataset for model training. This dual-
264 track analysis enables a clear distinction between the impacts of climate variability and emission
265 mitigation on observed ozone trends.

266 To examine the sensitivity of urban ozone pollution to climate variability under different potential
267 atmospheric conditions (e.g., oxidation capacity) and its possible evolution under global warming, we
268 defined three representative regional scenarios based on typical ozone pollution characteristics in China
269 (Fig. 3a): a high-pollution scenario for BTH (BaseBTH), a moderate-pollution scenario for YRD
270 (BaseYRD), and a low-pollution scenario for Pearl River Delta (PRD) (BasePRD). These scenarios allow
271 assessment of ozone trends and climate impacts under fixed emissions across three distinct atmospheric
272 conditions.

273 **3 Results and Discussion**274 **3.1 Spatiotemporal variation of summertime ozone**

275 Figure 3 presents the spatial distribution of the average summertime (2018-2023) maximum daily
 276 8-hour average (MDA8) ozone, surface NO_2 , and TROPOMI NO_2 , HCHO column concentrations across
 277 China, along with the locations of the country's five typical city clusters: BTH, Fenwei Plain (FWP),
 278 YRD, Sichuan Basin (SCB), and PRD. Across these five city clusters, the average summer ozone
 279 concentrations ranged from 88.9 to $161.3 \mu\text{g m}^{-3}$ – substantially exceeding the $43.0 \mu\text{g m}^{-3}$ threshold
 280 associated with ecosystem productivity loss (Gong et al., 2021) and the World Health Organization
 281 (WHO, 2021) recommended peak seasonal average of $60 \mu\text{g m}^{-3}$. TROPOMI satellite observations of
 282 NO_2 column concentration show notably elevated concentrations over the five city clusters, particularly
 283 in the BTH, YRD, and FWP, which align with surface NO_2 distribution patterns and confirm the scale of
 284 anthropogenic NO_x emissions in these regions (Zheng et al., 2021). TROPOMI satellite observations of
 285 HCHO column concentrations similarly reveal these city clusters as hotspots for VOC emissions (Fig.
 286 3d). These concurrent high levels of NO_2 and HCHO suggest a strong photochemical ozone pollution
 287 potential, as the abundant precursors in these urban clusters could drive substantial ozone production
 288 during the summer months.



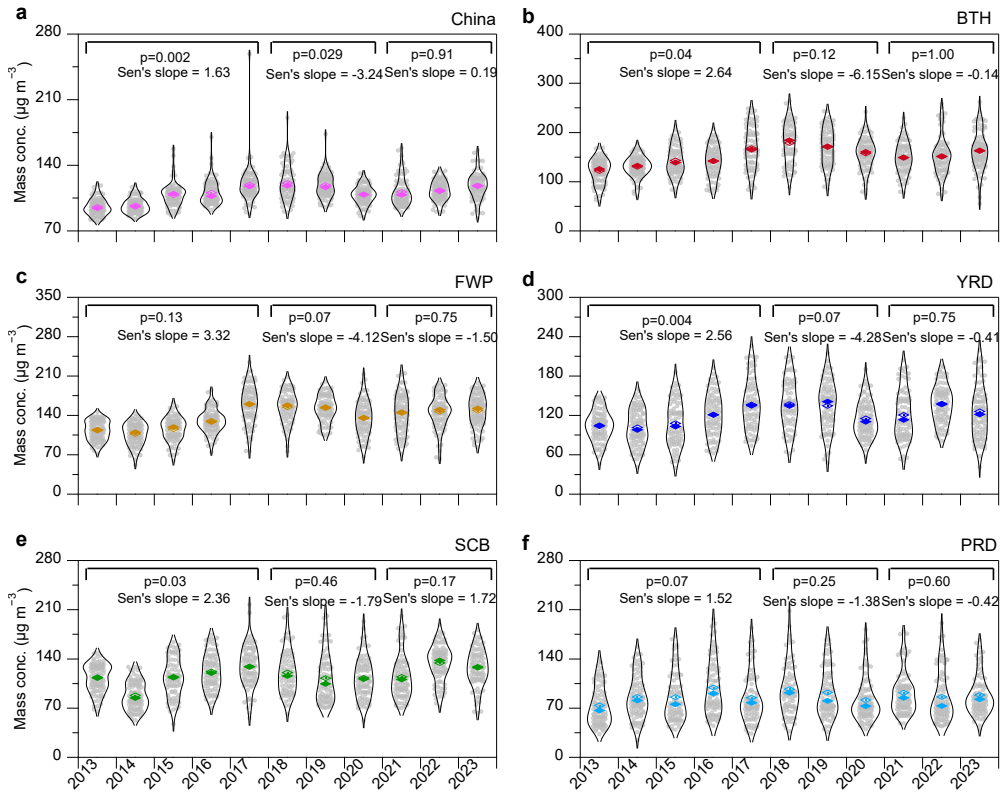
289 **Figure 3. Spatial distribution of summertime MDA8 ozone, surface NO_2 , and TROPOMI NO_2 , HCHO across**
 290 **major city clusters in China.** The panels represent the average MDA8 ozone, surface NO_2 , and TROPOMI NO_2 ,
 291 HCHO column concentrations for 354 cities in China during the summertime (June–August) from 2018 to 2023.
 292 The corresponding five regions includes BTH (37° – 41° N, 114° – 118° E); YRD (30° – 33° N, 118.2° – 122° E); SCB

294 (28.5°–31.5°N, 103.5°–107°E); PRD (21.5°–24°N, 112°–115.5°E) and FWP (106.25°–111.25°E, 33°–35°N, and
295 108.75°–113.75°E, 35°–37°N).

296

297 Figure 4 presents the interannual variations in MDA8 ozone concentrations during summertime
298 across China, with a focus on the five city cluster regions. During the Phase I (2013–2017), the average
299 nationwide MDA8 ozone increased significantly ($p < 0.01$), rising from 95.5 to 118.0 $\mu\text{g m}^{-3}$. This growth
300 was especially pronounced in the BTH and FWP regions, where the concentrations increased by
301 approximately 38% and 41%, respectively. In contrast, ozone increases were more modest in the YRD
302 (~11%), SCB (~15%), and PRD (~16%) regions, respectively. These results were consistent with the
303 previous studies (Li et al., 2021; Liu and Wang, 2020a, 2020b; Wang et al., 2023a). Corresponding to the
304 implementation of more stringent emission controls on NO_x and VOCs emissions during the Phase II
305 (Geng et al., 2024; Liu et al., 2023), a moderate national decrease in MDA8 ozone was observed, with
306 concentrations declining to 109.0 $\mu\text{g m}^{-3}$ from 2017 to 2020. The declines during this period were most
307 notable in FWP (~16%) and YRD (~15%), while BTH (~6%), SCB (~11%), and PRD (~4%) also showed
308 reductions compared to their concentration peaks observed in 2017. However, the MDA8 ozone
309 rebounded, reaching 118.4 $\mu\text{g m}^{-3}$ in 2023 – comparable to its 2017 peak – with a particularly sharp
310 increase during the summer of 2022. From 2021 to 2023, MDA8 ozone concentrations rose by 2.8 $\mu\text{g m}^{-3}$
311 in BTH, 3.1 $\mu\text{g m}^{-3}$ in FWP, 16.1 $\mu\text{g m}^{-3}$ in YRD, and 18.5 $\mu\text{g m}^{-3}$ in SCB, respectively.

312 Figure S1 further illustrates the spatiotemporal evolution of summertime MDA8 ozone in China
313 from 2013 to 2023. On average, approximately 68% of the cities exceeded the WHO air quality guideline
314 of 100 $\mu\text{g m}^{-3}$ for the MDA8 ozone. Elevated ozone levels were primarily observed in densely populated
315 and economically developed regions. Spatially, ozone hotspot regions expanded between 2013 and 2017
316 (Fig. S1 a–e), followed by contraction during 2018–2020 (Fig. S1 f–i). However, this progress stalled in
317 2021. A sharp reversal was observed in 2022, with widespread increases in MDA8 ozone (Fig. S1 k).
318 These changes could be closely linked to emission control measures and meteorological conditions,
319 which will be further discussed in Sections 3.2 and 3.3.



320

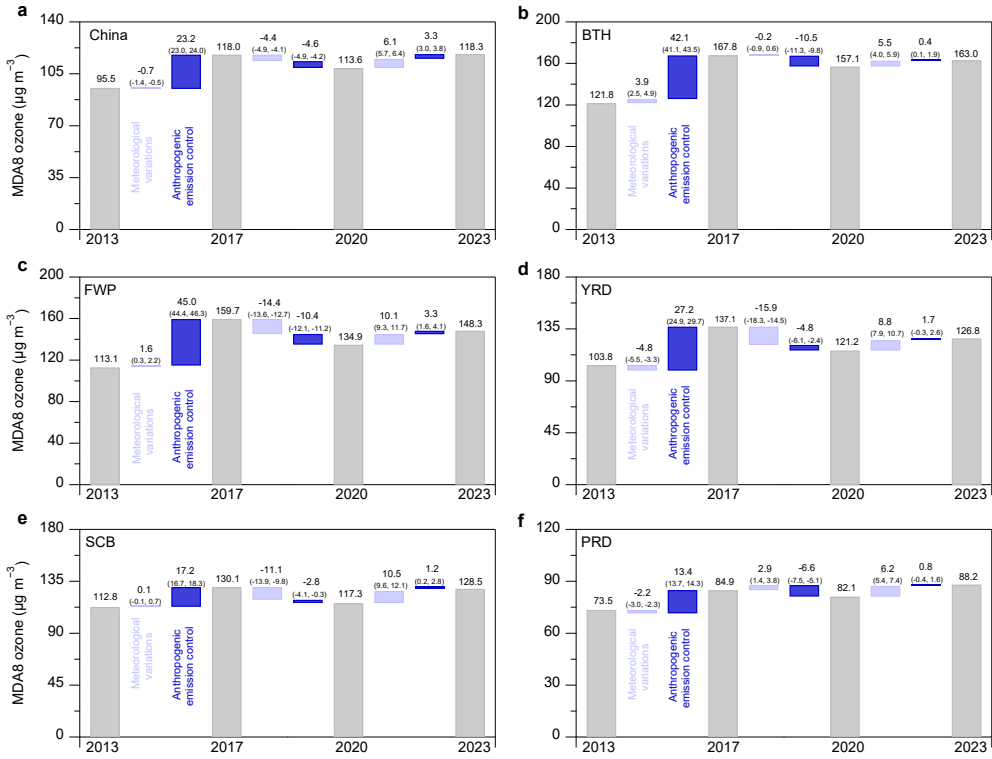
321 **Figure 4. Interannual trends of summertime MDA8 ozone across China (2013–2023).** **a** the seasonal variations
 322 of MDA8 ozone during the summer months (June, July, and August) over China. **b-f** the average trend across the
 323 five city cluster regions in China: BTH, FWP, YRD, SCB, and PRD, respectively. The summer months are defined
 324 according to meteorological seasonality, encompassing June, July, and August. In the violin plots, hollow diamond
 325 markers denote the mean, while solid diamond markers represent the median. The Mann-Kendall test and Sen's slope
 326 estimator were employed to assess the statistical significance and rate of change in the monthly average MDA8
 327 ozone concentrations. The *p* value represents the significance level from the Mann-Kendall test, which is used to
 328 determine the statistical significance of the trend in the data.

329

330 3.2 Anthropogenic emission drivers of ozone trends

331 To disentangle the relative impacts of anthropogenic emissions and meteorological variability on
 332 observed ozone trends, we applied the machine learning-based FEA framework described in Section 2.2.
 333 As illustrated in Fig. 5, anthropogenic emissions were the dominant driver of ozone increases during
 334 2013–2017, contributing an average rise of approximately $23.2 \pm 1.1 \mu\text{g m}^{-3}$ nationwide. The most
 335 pronounced increases occurred in the FWP and BTH ($45.0 \pm 2.0 \mu\text{g m}^{-3}$ and $42.1 \pm 2.0 \mu\text{g m}^{-3}$,
 336 respectively), whereas the PRD exhibited a relatively modest enhancement ($13.4 \pm 1.6 \mu\text{g m}^{-3}$), reflecting
 337 its predominantly NO_x -limited photochemical regime versus VOC-limited regimes in other regions (Ren
 338 et al., 2022). As shown in Fig. S5, the precursor gases NO_2 and CO exhibited regionally distinct

339 decreasing trends, partially explaining the spatial heterogeneity of ozone changes. The MDA8 ozone
340 decreased by $10.5 \pm 2.0 \mu\text{g m}^{-3}$ in BTH and $10.4 \pm 3.0 \mu\text{g m}^{-3}$ in FWP, with smaller declines in YRD ($-4.8 \pm 3.8 \mu\text{g m}^{-3}$), SCB ($-2.8 \pm 2.4 \mu\text{g m}^{-3}$), and PRD ($-6.6 \pm 1.4 \mu\text{g m}^{-3}$) between 2017 and 2020 (Fig. 5).
341 These trends were overall consistent with those derived using independent statistical approaches (Wang
342 et al., 2023). The COVID-19 pandemic (January-April 2020) introduced an unprecedented perturbation
343 to anthropogenic activity, leading to sharp declines in industrial production, energy consumption, and
344 transportation (Shi and Brasseur, 2020; Zheng et al., 2021). National emissions of SO_2 , NO_x , $\text{PM}_{2.5}$, and
345 VOCs were estimated to have decreased by 0.37 Tg (12%), 0.87 Tg (13%), 0.25 Tg (10%), and 1.07 Tg
346 (12%), respectively, relative to the same period in 2019 (Geng et al., 2024). Despite these reductions,
347 MDA8 ozone concentrations increased by $1.7\text{--}2.3 \mu\text{g m}^{-3}$ across BTH, FWP, YRD, and SCB, while a
348 slight decrease occurred in PRD (Fig. S6). Overall, $\sim 79\%$ of monitored cities experienced ozone
349 increases, with a national mean enhancement of $2.1 \pm 1.3 \mu\text{g m}^{-3}$ (Fig. S7). In the post-pandemic period
350 (2020–2023), concentrations of NO_2 , CO, and $\text{PM}_{2.5}$ stabilized or declined more gradually (Fig. S5), and
351 the contribution of anthropogenic emissions to ozone variability weakened considerably (Fig. S8).
352 Regionally, emission-driven changes ranged from -1.2 to $+2.6 \mu\text{g m}^{-3}$ in BTH, -1.6 to $+4.0 \mu\text{g m}^{-3}$ in
353 FWP, -4.7 to $+7.4 \mu\text{g m}^{-3}$ in YRD, -3.6 to $+3.0 \mu\text{g m}^{-3}$ in SCB, and -3.8 to $+7.7 \mu\text{g m}^{-3}$ in PRD. These
354 results indicate that while emission controls initially yielded substantial ozone mitigation benefits during
355 the Phase II, their effectiveness has gradually diminished, underscoring the need for more targeted and
356 region-specific emission control strategies under evolving photochemical regimes.
357



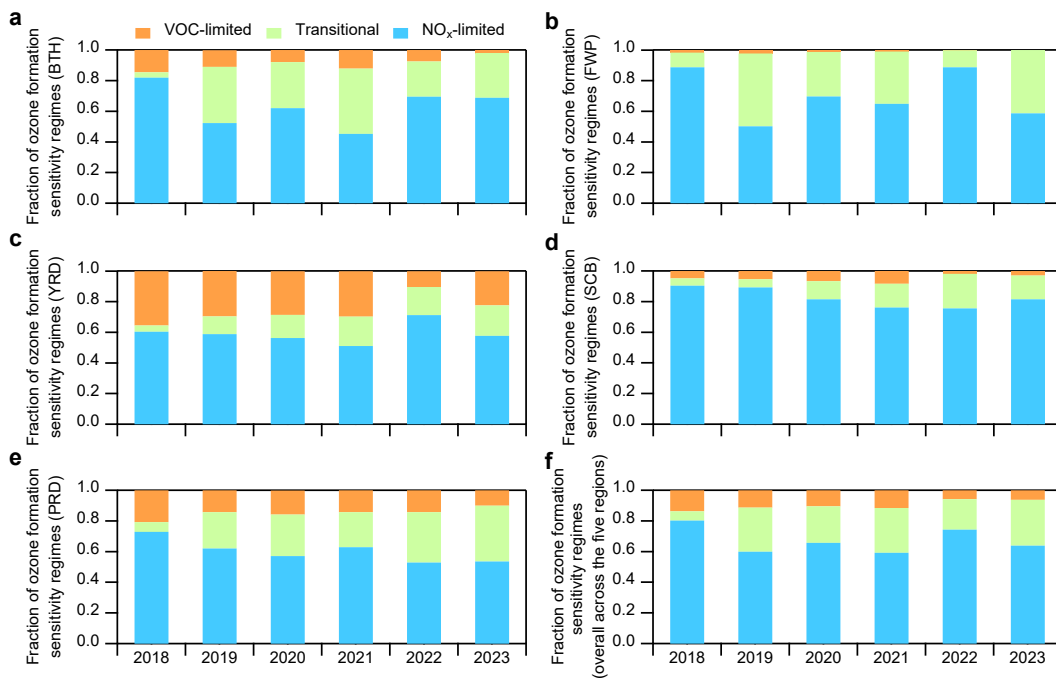
358

359 **Figure 5. Anthropogenic and meteorological drivers of ozone trends from 2013 to 2023.** Changes in summertime
360 MDA8 ozone concentrations were decomposed into contributions from anthropogenic emissions and meteorological
361 variability using the FEA framework. Results reflect ensemble estimates based on multiple baseline years (2015–
362 2023) for emissions. The interquartile range, with values in parentheses denoting the 25th and 75th percentiles across
363 all baseline scenarios.

364

365 Satellite retrievals of tropospheric NO₂ and HCHO from TROPOMI (Figs. S9–S10) further reveal
366 evolving ozone production chemistry. NO₂ columns exhibited strong east–west gradients, with eastern
367 China maintaining levels five times higher than the west. Between 2018 and 2023, NO₂ columns over
368 the North China Plain (NCP) declined from 4.13×10^{15} to 3.85×10^{15} molecules cm⁻², while HCHO
369 remained stable until 2021, followed by a sharp increase in 2022. The spatial pattern of temperature
370 anomalies between heatwave and non-heatwave periods (Fig. S11) reveals strong positive differences in
371 the YRD and SCB, consistent with enhanced biogenic and anthropogenic VOC emissions under extreme
372 heat (Qin et al., 2025; Tao et al., 2024). By 2023, HCHO concentrations had returned to pre-heatwave
373 levels. To diagnose the evolving chemical sensitivity of ozone production, we examined the
374 spatiotemporal evolution of the HCHO/NO₂ ratio (Text S1). Figure S12 shows that this ratio exhibited
375 regionally distinct transitions from 2018 to 2023, reflecting shifts in photochemical regimes. Figure 6
376 summarizes the relative contributions of VOC-limited, NO_x-limited, and transitional regimes across the
377 five key regions. In BTH, NO_x-limited areas accounted for ~82% of the domain in 2018 and remained

378 above 45% thereafter, while VOC-limited regions declined from ~14% to ~2%. In FWP, summertime
 379 ozone formation was largely controlled by NO_x-limited and transitional regimes. The YRD underwent a
 380 notable shift from VOC- to NO_x-limited chemistry, with VOC-limited fractions decreasing from ~35%
 381 in 2018 to ~22% in 2023, particularly during 2022 when extreme heat amplified VOC emissions and
 382 photochemical activity (Qin et al., 2025; Tao et al., 2024). The SCB region consistently exhibited strong
 383 NO_x limitation (>75%), whereas the PRD showed a gradual expansion of the transitional regime
 384 alongside a modest contraction of VOC-limited regions. These shifts in photochemical sensitivity
 385 correspond well with the ozone decrease observed during the Phase II emission reductions. Spatial
 386 distributions of ozone formation sensitivity during the COVID-19 lockdown (Fig. S13) reveal that most
 387 of China was in a transitional regime, with major urban clusters remaining VOC-limited and only limited
 388 areas in southern China being NO_x-limited. This spatial pattern aligns with the observed widespread
 389 ozone increases during the lockdown (Fig. S7). These findings highlight that ozone production chemistry
 390 in China was shaped by the complex interplay between emission reduction efforts and the rising
 391 frequency of meteorological extremes under a warming climate.



392
 393 **Figure 6. Trends in the distributions of ozone production sensitivity regimes.** Fractions of VOC-limited, NO_x-
 394 limited, and transitional ozone sensitivity regimes across five key regions during the summertime (June to August)
 395 from 2018 to 2023, based on the FNR analysis. **a-e** the trend across the five city cluster regions in China during the
 396 summer months (June, July, and August): BTH, FWP, YRD, SCB, and PRD, respectively. **f** the overall trends for all
 397 five regions.

398 **3.3 Meteorological impact on ozone variation**

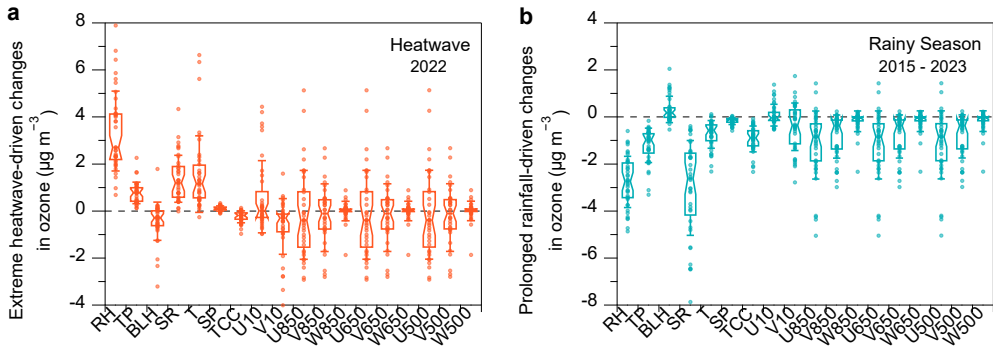
399 Figure 5 shows the interannual meteorological contributions to summertime MDA8 ozone across
400 different emission-control phases. During the Phase I, meteorology exerted relatively weak influences
401 on ozone variability, with contributions ranging from -4.8 to $+3.9 \mu\text{g m}^{-3}$ —far smaller than those from
402 anthropogenic emission changes. In contrast, meteorological anomalies became a decisive factor from
403 2017 to 2020, driving substantial ozone reductions. Ozone decreases attributable to meteorology reached
404 $-14.4 \pm 3.0 \mu\text{g m}^{-3}$ in the FWP, $-15.9 \pm 3.8 \mu\text{g m}^{-3}$ in the YRD, and $-11.1 \pm 2.4 \mu\text{g m}^{-3}$ in the SCB,
405 explaining $58 \pm 12\%$, $77 \pm 18\%$, and $80 \pm 17\%$ of the total ozone decline, respectively. A notable shift
406 occurred from 2020 to 2023, when the influence of extreme meteorological events increasingly
407 dominated ozone variability. In the summer of 2022, persistent heatwaves across eastern and southern
408 China (Mallapaty, 2022; Wang et al., 2023b) triggered sharp ozone increases of $+20.8 \pm 3.6 \mu\text{g m}^{-3}$ in
409 the YRD and $+22.1 \pm 3.2 \mu\text{g m}^{-3}$ in the SCB, reflecting the enhanced photochemical activity under high-
410 temperature and intense solar radiation conditions. The following summer (2023) featured anomalously
411 heavy rainfall, resulting in sharp ozone suppression ($-17.8 \pm 2.3 \mu\text{g m}^{-3}$ in the YRD and $-9.7 \pm 3.3 \mu\text{g}$
412 m^{-3} in the SCB). This reduction coincided with a remarkable increase in precipitation, i.e., 102% in YRD
413 and 35% in SCB (Fig. S14), indicating that rainy meteorological conditions may have suppressed ozone
414 production.

415 To identify the dominant meteorological drivers, we analyzed Gini importance scores derived from
416 the RF model across 18 predictor variables (Fig. S15). Temperature (T) emerged as the most influential
417 predictor in the BTH and FWP regions, while shortwave solar radiation (SR), relative humidity (RH),
418 and 850hPa zonal wind (u850) were most important in the YRD. In the PRD, ozone variability was
419 primarily governed by temperature and transport-related indices, including meridional winds at different
420 altitudes. These findings are consistent with the climatological contrast between northern continental and
421 southern coastal regimes: in northern China, stagnant anticyclonic conditions (Gong and Liao, 2019) and
422 strong solar radiation promote photochemical production (Bao et al., 2025), whereas in southern regions,
423 high humidity and convective rainfall could tend to suppress ozone by reducing actinic flux and
424 enhancing removal of precursors(Lu et al., 2019).

425 Partial dependence analysis (Fig. S16) further illustrates the nonlinear responses of ozone to key
426 meteorological factors (T, RH, and SR) for representative cities in each cluster, revealing clear regional

427 contrasts. In Beijing (BTH), ozone concentrations show the strongest positive response to T (Fig. S16a),
428 consistent with the enhancement of reaction kinetics and biogenic VOC emissions under hot conditions.
429 This behavior reflects the thermodynamic coupling between surface heating, boundary-layer expansion,
430 and photochemical production. In Nanjing (YRD), ozone was more sensitive to solar radiation than to
431 temperature (Fig. S16c), highlighting the dominant role of actinic flux in controlling radical production
432 during warm and dry conditions. Consistent with these findings, Yang et al. (2024) reported that high-
433 temperature and low-RH conditions over the NCP and YRD could enhance photochemical ozone
434 formation, with chemical production dominating during peak pollution periods. In the SCB, both T and
435 RH exhibited strong influences, while ozone variability was shaped primarily by T and large-scale
436 circulation patterns in the PRD associated with subtropical maritime flow and typhoon incursions from
437 the Northwest Pacific (Chen et al., 2024; Wang et al., 2024a; Wang et al., 2022a).

438 To further quantify these relationships, we applied SHAP (SHapley Additive exPlanations) analysis
439 to evaluate the meteorological influence of the HW and the PR events in the Yangtze-Huaihe region
440 between 2015 and 2023 (Section 2.4). As shown in Fig. S17, the HW events were associated with strong
441 positive SHAP values in southeastern coastal areas, especially the YRD and SCB, driven by elevated SR
442 and T . Mean SR during the HW periods was substantially higher than during the NHW periods (Fig.
443 S18), increasing photochemical activity through increased radical generation and faster reaction rates.
444 Conversely, PR events produced consistent negative SHAP contributions across all regions (Fig. S19),
445 reflecting the combined effects of reduced photolysis, increased humidity, and efficient wet scavenging
446 on ozone production (He and Carmichael, 1999). A multi-year comparison (Fig. 7) highlights the
447 opposing effects of key meteorological variables – including RH, T , boundary layer height (BLH), total
448 precipitation (TP), and surface pressure (SP) – on MDA8 ozone. The trend in Δ SHAP values under
449 high-humidity conditions from 2015 to 2023 (Fig. S20) further confirms the model’s ability to capture
450 the suppressive effects of wet weather conditions on ozone formation.



451 **Figure 7. Meteorological impact on predicted ozone concentrations under heatwave and rainy weather**
452 **conditions.** **a** the differences in SHAP values (Δ SHAP) between heatwave and non-heatwave periods in the Yangtze-
453 Huaihe region during summer 2022. **b** the Δ SHAP between prolonged rainfall periods and non-prolonged rainfall
454 periods in the same region from 2015 to 2023. Box plots show the distribution of Δ SHAP across cities; the center
455 line indicates the median, boxes denote the interquartile range (25th-75th percentiles), and the whisker line extends
456 to one standard deviation.

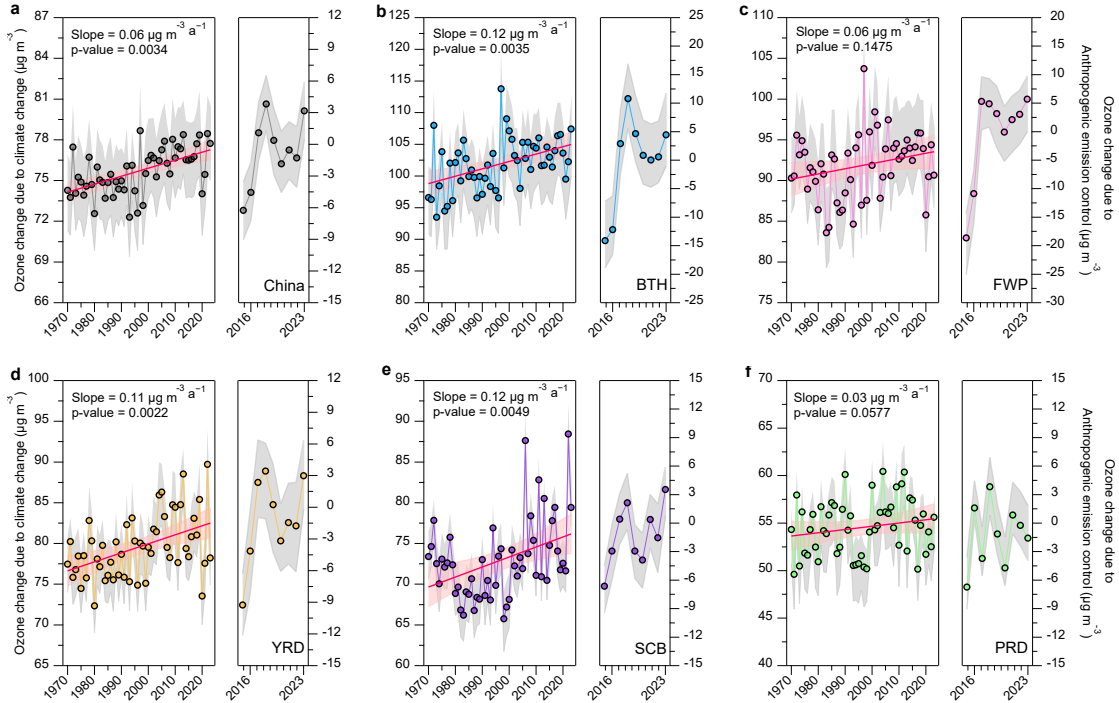
457 **3.4 Reshaping distributions of ozone by climate change and emission controls**

458 To assess the long-term influence of climate change on surface ozone concentrations, we applied
459 the FEA framework to simulate summertime ozone trends over the period 1970 – 2023. In this analysis,
460 anthropogenic emissions were held constant at their 2015 – 2023 summertime levels, while interannual
461 variations in meteorological variables were introduced using historical reanalysis data. This design
462 isolates the climate-driven component of ozone trends while assuming that emission trajectories are
463 independent of climate change – a simplification aligned with prior attribution frameworks (Wang et al.,
464 2022b). The impact of anthropogenic emission controls was estimated by comparing observed ozone
465 concentrations with FEA-predicted values during 2015 – 2023, thereby quantifying the residual effect of
466 emissions under fixed meteorology.

467 As shown in Fig. 8, under the 2015-2023 emission levels, climate change has exerted a statistically
468 significant ($p < 0.05$) positive influence on urban summertime ozone concentrations across China,
469 resulting in a nationwide increase of approximately $0.06 \mu\text{g m}^{-3} \text{ yr}^{-1}$ since 1970. All five major urban
470 regions displayed upward trends, with the most pronounced increase observed in the BTH and SCB at
471 $0.12 \mu\text{g m}^{-3} \text{ yr}^{-1}$. Three sensitivity simulations (see Section 2.5 and Fig. S21) confirm this robustness:
472 trend slopes range from $0.11\text{--}0.14 \mu\text{g m}^{-3} \text{ yr}^{-1}$ in BaseBTH (high-pollution scenario), $0.05\text{--}0.10 \mu\text{g m}^{-3}$
473 yr^{-1} in the BaseYRD (moderate-pollution scenario), and $0.03\text{--}0.10 \mu\text{g m}^{-3} \text{ yr}^{-1}$ in the BasePRD (low-
474 pollution scenario). Despite regional differences in chemical regimes or pollution levels, the consistent

477 upward tendencies underscore the pervasive climatic amplification of ozone formation. These results
478 emphasize that climate change acts as a systematic driver of ozone growth across diverse atmospheric
479 environments, reinforcing the need to embed climate resilience within emission control strategies. Spatial
480 correlations between climate-driven ozone increases and temperature changes (Fig. S22) further confirm
481 that warming is the dominant contributor to long-term ozone enhancement. In particular, the correlation
482 coefficients between ozone trends and temperature anomalies reached 0.90 (BTH), 0.89 (FWP), 0.72
483 (YRD), and 0.93 (SCB), indicating a strong temperature dependence of climate-induced ozone formation
484 in these regions. The PRD showed a weaker correlation, likely due to its unique subtropical maritime
485 climate and higher humidity and cloud cover, which tend to suppress photochemical ozone production
486 (Yang et al., 2019). The right panel of Fig. 8 depicts summertime ozone trends from 2015 to 2023 under
487 the combined influence of anthropogenic emissions, derived from the FEA method. Ozone
488 concentrations rose across all regions between 2015 and 2018, declined modestly during 2018-2020, and
489 rebounded thereafter in most regions except the PRD.

490 These findings are consistent with future projections that anticipate more frequent high-ozone
491 episodes under continued warming (Li et al., 2023). Recent analyses (Yang et al., 2024) show that the
492 frequency of high-temperature and low-humidity conditions during 2000-2019 was markedly higher than
493 in 1980-1999, suggesting that ozone pollution in both the NCP and YRD has intensified under historical
494 climate change. Indeed, while national emission controls curbed ozone growth after 2018, a post-2020
495 rebound has emerged, implying that the climatic penalty on ozone is beginning to offset emission gains.
496 The extreme 2022 heatwave exemplified this effect, substantially enhancing photochemical activity and
497 shifting ozone sensitivity from VOC-limited to transitional or NO_x-limited regimes. Although reductions
498 in anthropogenic precursor emissions have improved ozone control efficiency, the warming-induced
499 enhancement of ozone increasingly interferes with – and in some regions may partially offset – the air-
500 quality gains achieved through emission reduction efforts.



501

502 **Figure 8. Impact of climate change and emission controls on ozone trends.** Left panels show ozone trends
 503 attributable to long-term climate change from 1970 to 2023, simulated under fixed emission scenarios using the FEA
 504 framework. Right panels depict ozone trends from 2015 to 2023, reflecting the impact of anthropogenic emission
 505 controls. Each trajectory represents results based on a distinct emissions baseline year. Shaded grey areas indicate
 506 the interquartile range (25th-75th percentiles), solid red lines denote trend estimates, and light red shading marks the
 507 5th-95th percentile confidence intervals. Statistical significance and trend slopes were assessed using the Mann-
 508 Kendall test. More details of the sensitivity tests are provided in Fig. S18.

509

4 Conclusions and implications

510 In this study, we developed a machine learning-based FEA framework to disentangle and quantify the
 511 respective roles of anthropogenic emissions and meteorological drivers in shaping ozone trends during
 512 2013-2023. With a national-level prediction uncertainty of approximately 6%, the FEA method provides
 513 a computationally efficient and scalable tool for diagnosing atmospheric variability across large spatial
 514 and temporal domains. However, the current model framework did not explicitly resolve grid-scale
 515 spatial heterogeneity, vegetation feedbacks, or land-use dynamics, which may influence the ozone
 516 prediction. In addition, the sensitivity of the results to spatial resolution need further investigation
 517 through coupled applications of machine learning and chemical transport models.

518

Our results revealed that increased anthropogenic emissions were the dominant driver of the sharp
 519 rise in summertime MDA8 ozone concentrations during the Phase I, contributing an average increase of

520 $23.2 \pm 1.1 \text{ } \mu\text{g m}^{-3}$. In contrast, the strengthened clean air actions during the Phase II – particularly the
521 synergistic control of NO_x and VOCs – led to measurable reductions in MDA8 ozone, with national-
522 average declines of $4.6 \pm 1.5 \text{ } \mu\text{g m}^{-3}$ from 2017 to 2020. These improvements were especially evident in
523 regions such as BTH and FWP, where ozone formation was highly sensitive to VOCs. However, the
524 impact of emission reductions diminished considerably during the recent period (2021–2023). This
525 stagnation underscores the urgent need for more targeted, region-specific emission control strategies that
526 address the shifting photochemical sensitivity of ozone formation regimes.

527 Using the SHAP attribution analysis, we further quantified the influence of meteorological extremes
528 on ozone variability. Record-breaking heatwaves in 2022 enhanced ozone concentrations by up to $+5.8$
529 $\mu\text{g m}^{-3}$, while prolonged pluvial episodes, particularly during the East Asian monsoon season, suppressed
530 ozone by as much as $-15.2 \mu\text{g m}^{-3}$. These results highlight the dominance of short-term meteorological
531 extremes in shaping ozone air quality under a warming climate. Complementary satellite-based FNR
532 diagnostics revealed that from 2018 to 2023, summertime ozone formation was predominantly
533 influenced by NO_x -limited and transitional regimes, while VOC-limited areas experienced a decline. The
534 2022 heatwave induced regime shifts in regions such as the YRD, where intensified VOC emissions and
535 elevated temperatures drove transitions toward NO_x -limited conditions. These findings emphasize the
536 need for dynamic, region-specific assessments of ozone sensitivity to guide effective mitigation strategies.

537 To assess the climate penalty on ozone, we extended the FEA framework to simulate long-term
538 trends from 1970 to 2023 by fixing emissions and allowing meteorological variables to evolve with
539 observed climate trends. Our findings show that climate change has contributed to a significant upward
540 trend in urban summertime ozone, averaging $0.06 \mu\text{g m}^{-3} \text{ yr}^{-1}$, with particularly strong increases in the
541 BTH and SCB. Good correlations between the modelled ozone and surface temperature ($r = 0.72\text{--}0.93$)
542 across major urban clusters indicated that climate warming exerts a persistent control on the long-term
543 evolution of ozone. While reductions in precursor emissions have improved ozone control efficiency, the
544 direct enhancement of ozone by rising temperatures increasingly interferes with, and in some regions
545 may partially offset, the air-quality benefits achieved through emission mitigation. Together, these
546 findings highlight that effective ozone management in a warming world will require integrated strategies
547 that jointly address emission reductions and climate adaptation.

548

549 *Data availability.* Data are provided within the manuscript or supplementary information files.

550

551 *Code availability.* The statistical computing in this study was based on R language software which can
552 be download at <https://www.r-project.org/>.

553

554 *Author contributions.*

555 Y.Z. initiated and designed the study. Y.Z. and JF developed the statistical methodology, model
556 calculation, and data analysis. J.F. and Y.Z. prepared the manuscript with contributions from D.H., B.Z.,
557 M.W., J.L., Y.S., H.L., J.W., Y.W., B.Y., M.C., and X.G..

558

559 *Competing interests.* The authors declare no competing interests.

560

561 *Acknowledgments.*

562 This study was supported by the National Key Research and Development Program of China (grant
563 2023YFC3706200), the National Natural Science Foundation of China (grant no. 42207124) and Natural
564 Science Foundation of Jiangsu Province (grant no. BK20210663).

565

566 **Correspondence** and requests for materials should be addressed to Yunjiang Zhang.

567

568 **References**

569 Agathokleous, E., Feng, Z., Oksanen, E., Sicard, P., Wang, Q., Saitanis, C.J., Araminiene, V., Blande,
570 J.D., Hayes, F., Calatayud, V., Domingos, M., Veresoglou, S.D., Peñuelas, J., Wardle, D.A., De Marco,
571 A., Li, Z., Harmens, H., Yuan, X., Vitale, M., Paoletti, E.: Ozone affects plant, insect, and soil microbial
572 communities: A threat to terrestrial ecosystems and biodiversity, *Sci. Adv.*, 6, eabc1176,
573 <https://doi.org/10.1126/sciadv.abc1176>, 2020.

574 Bao, J., Li, X., Kong, L., Li, J., Chen, Q., Zhang, Y.: Comparative analysis of the impact of rising
575 temperatures on ozone levels in China and the United States, *npj Clean Air*, 1, 23,
576 <https://doi.org/10.1038/s44407-025-00023-8>, 2025.

577 Chen, S., Wang, H., Lu, K., Zeng, L., Hu, M., Zhang, Y.: The trend of surface ozone in Beijing from 2013
578 to 2019: Indications of the persisting strong atmospheric oxidation capacity, *Atmos. Environ.*, 242,
579 117801, <https://doi.org/10.1016/j.atmosenv.2020.117801>, 2020.

580 Chen, Y., Lu, X., Fung, J.C.H.: Spatiotemporal source apportionment of ozone pollution over the Greater
581 Bay Area, *Atmos. Chem. Phys.*, 24, 8847-8864, <https://doi.org/10.5194/acp-24-8847-2024>, 2024.

582 Dai, Q., Dai, T., Hou, L., Li, L., Bi, X., Zhang, Y., Feng, Y.: Quantifying the impacts of emissions and
583 meteorology on the interannual variations of air pollutants in major Chinese cities from 2015 to 2021,
584 *Sci. China Earth Sci.*, 66, 1725-1737, <https://doi.org/10.1007/s11430-022-1128-1>, 2023.

585 Dang, R., Liao, H.: Severe winter haze days in the Beijing–Tianjin–Hebei region from 1985 to 2017 and
586 the roles of anthropogenic emissions and meteorology, *Atmos. Chem. Phys.*, 19, 10801-10816,
587 <https://doi.org/10.5194/acp-19-10801-2019>, 2019.

588 Fishman, J., Ramanathan, V., Crutzen, P.J., Liu, S.C.: Tropospheric ozone and climate, *Nature*, 282, 818-
589 820, <https://doi.org/10.1038/282818a0>, 1979.

590 Gao, M., Wang, F., Ding, Y., Wu, Z., Xu, Y., Lu, X., Wang, Z., Carmichael, G.R., McElroy, M.B.: Large-
591 scale climate patterns offer preseasonal hints on the co-occurrence of heat wave and O₃ pollution in
592 China, *Proc. Natl. Acad. Sci. USA*, 120, e2218274120, <https://doi.org/10.1073/pnas.2218274120>,
593 2023.

594 Geng, G., Liu, Y., Liu, Y., Liu, S., Cheng, J., Yan, L., Wu, N., Hu, H., Tong, D., Zheng, B., Yin, Z., He,
595 K., Zhang, Q.: Efficacy of China's clean air actions to tackle PM_{2.5} pollution between 2013 and 2020,
596 *Nat. Geosci.*, 17, 987-994, <https://doi.org/10.1038/s41561-024-01540-z>, 2024.

597 Geng, G., Xiao, Q., Liu, S., Liu, X., Cheng, J., Zheng, Y., Xue, T., Tong, D., Zheng, B., Peng, Y., Huang,
598 X., He, K., Zhang, Q.: Tracking air pollution in China: Near real-time PM_{2.5} retrievals from
599 multisource data fusion, *Environ. Sci. Technol.*, 55, 12106-12115,
600 <https://doi.org/10.1021/acs.est.1c01863>, 2021.

601 Gong, C., Liao, H.: A typical weather pattern for ozone pollution events in North China, *Atmos. Chem.*
602 *Phys.*, 19, 13725-13740, <https://doi.org/10.5194/acp-19-13725-2019>, 2019.

603 Gong, C., Yue, X., Liao, H., Ma, Y.M.: A humidity-based exposure index representing ozone damage
604 effects on vegetation, *Environ. Res. Lett.*, 16, <https://doi.org/10.1088/1748-9326/abecbb>, 2021.

605 Grange, S.K., Carslaw, D.C., Lewis, A.C., Boleti, E., Hueglin, C.: Random forest meteorological
606 normalisation models for Swiss PM₁₀ trend analysis, *Atmos. Chem. Phys.*, 18, 6223-6239,
607 <https://doi.org/10.5194/acp-18-6223-2018>, 2018.

608 Guo, J., Zhang, X., Gao, Y., Wang, Z., Zhang, M., Xue, W., Herrmann, H., Brasseur, G.P., Wang, T.,
609 Wang, Z.: Evolution of ozone pollution in China: what track will it follow? *Environ. Sci. Technol.*, 57,
610 109-117, <https://doi.org/10.1021/acs.est.2c08205>, 2023.

611 Hallquist, M., Munthe, J., Hu, M., Wang, T., Chan, C.K., Gao, J., Boman, J., Guo, S., Hallquist, Å.M.,
612 Mellqvist, J., Moldanova, J., Pathak, R.K., Pettersson, J.B.C., Pleijel, H., Simpson, D., Thynell, M.:
613 Photochemical smog in China: scientific challenges and implications for air-quality policies, *Natl. Sci.*
614 *Rev.*, 3, 401-403, <https://doi.org/10.1093/nsr/nww080>, 2016.

615 Hauglustaine, D.A., Granier, C., Brasseur, G.P., Mégie, G.: The importance of atmospheric chemistry in
616 the calculation of radiative forcing on the climate system, *J. Geophys. Res.*, 99, 1173-1186,
617 <https://doi.org/10.1029/93JD02987>, 1994.

618 He, S., Carmichael, G.R.: Sensitivity of photolysis rates and ozone production in the troposphere to
619 aerosol properties, *J. Geophys. Res. Atmos.*, 104, 26307-26324.
620 <https://doi.org/10.1029/1999JD900789>, 1999.

621 IPCC, 2021. Annex I: Observational Products [Trewin, B. (ed.)], in: Masson-Delmotte, V., Zhai, P., Pirani,
622 A., Connors, S.L., Péan, C., Berger, S., Caud, N., Chen, Y., Goldfarb, L., Gomis, M.I., Huang, M.,
623 Leitzell, K., Lonnoy, E., Matthews, J.B.R., Maycock, T.K., Waterfield, T., Yelekçi, O., Yu, R., Zhou,
624 B. (Eds.), *Climate Change 2021: The Physical Science Basis. Contribution of Working Group I to the*
625 *Sixth Assessment Report of the Intergovernmental Panel on Climate Change*. Cambridge University
626 Press, Cambridge, United Kingdom and New York, NY, USA, pp. 2061–2086.

627 Ivatt, P.D., Evans, M.J., Lewis, A.C.: Suppression of surface ozone by an aerosol-inhibited
628 photochemical ozone regime, *Nat. Geosci.*, 15, 536-540, <https://doi.org/10.1038/s41561-022-00972-9>, 2022.

629 Jacob, D.J.: Heterogeneous chemistry and tropospheric ozone, *Atmos. Environ.*, 34, 2131-2159,
630 [https://doi.org/10.1016/S1352-2310\(99\)00462-8](https://doi.org/10.1016/S1352-2310(99)00462-8), 2000.

631 Knowlton, K., Rosenthal, J.E., Hogrefe, C., Lynn, B., Gaffin, S., Goldberg, R., Rosenzweig, C., Civerolo,
632 K., Ku, J.-Y., Kinney, P.L.: Assessing ozone-related health impacts under a changing climate, *Environ.*
633 *Health Perspect.*, 112, 1557-1563, <https://doi.org/10.1289/ehp.716>, 2004.

634 Lamsal, L.N., Krotkov, N.A., Celarier, E.A., Swartz, W.H., Pickering, K.E., Bucsela, E.J., Gleason, J.F.,
635 Martin, R.V., Philip, S., Irie, H., Cede, A., Herman, J., Weinheimer, A., Szykman, J.J., Knepp, T.N.:
636 Evaluation of OMI operational standard NO₂ column retrievals using in situ and surface-based NO₂
637 observations, *Atmos. Chem. Phys.*, 14, 11587-11609, <https://doi.org/10.5194/acp-14-11587-2014>,
638 2014.

639 Lecœur, È., Seigneur, C., Pagé, C., Terray, L.: A statistical method to estimate PM_{2.5} concentrations from
640 meteorology and its application to the effect of climate change, *J. Geophys. Res. Atmos.*, 119, 3537-
641 3585, <https://doi.org/10.1002/2013JD021172>, 2014.

642 Leung, D.M., Tai, A.P.K., Mickley, L.J., Moch, J.M., van Donkelaar, A., Shen, L., Martin, R.V.: Synoptic
643 meteorological modes of variability for fine particulate matter (PM_{2.5}) air quality in major metropolitan
644 regions of China, *Atmos. Chem. Phys.*, 18, 6733-6748, <https://doi.org/10.5194/acp-18-6733-2018>,
645 2018.

646 Li, H., Yang, Y., Jin, J., Wang, H., Li, K., Wang, P., Liao, H.: Climate-driven deterioration of future ozone
647 pollution in Asia predicted by machine learning with multi-source data, *Atmos. Chem. Phys.*, 23, 1131-
648 1145, <https://doi.org/10.5194/acp-23-1131-2023>, 2023.

649 Li, J., Wang, S., Zhu, J., Wang, D., Zhao, T.: Accelerated shifts from heatwaves to heavy rainfall in a
650 changing climate, *npj Clim. Atmos. Sci.* 8, 214, <https://doi.org/10.1038/s41612-025-01113-w>, 2025a.

651 Li, K., Jacob, D.J., Liao, H., Shen, L., Zhang, Q., Bates, K.H.: Anthropogenic drivers of 2013–2017
652 trends in summer surface ozone in China, *Proc. Natl. Acad. Sci. USA*, 116, 422-427,
653 <https://doi.org/10.1073/pnas.1812168116>, 2019a.

654

655 Li, K., Jacob, D.J., Liao, H., Zhu, J., Shah, V., Shen, L., Bates, K.H., Zhang, Q., Zhai, S.: A two-pollutant
656 strategy for improving ozone and particulate air quality in China, *Nat. Geosci.*, 12, 906-910,
657 <https://doi.org/10.1038/s41561-019-0464-x>, 2019b.

658 Li, K., Jacob, D.J., Shen, L., Lu, X., De Smedt, I., Liao, H.: Increases in surface ozone pollution in China
659 from 2013 to 2019: anthropogenic and meteorological influences, *Atmos. Chem. Phys.*, 20, 11423-
660 11433, <https://doi.org/10.5194/acp-20-11423-2020>, 2020.

661 Li, M., Wang, T., Shu, L., Qu, Y., Xie, M., Liu, J., Wu, H., Kalsoom, U.: Rising surface ozone in China
662 from 2013 to 2017: A response to the recent atmospheric warming or pollutant controls? *Atmos.*
663 *Environ.*, 246, 118130, <https://doi.org/10.1016/j.atmosenv.2020.118130>, 2021.

664 Li, S., Wu, L., Wang, Y., Geng, T., Cai, W., Gan, B., Jing, Z., Yang, Y.: Intensified Atlantic multidecadal
665 variability in a warming climate, *Nat. Clim. Change*, 15, 293-300, <https://doi.org/10.1038/s41558-025-02252-x>, 2025b.

666 Liu, C., Shi, K.: A review on methodology in O₃-NO_x-VOC sensitivity study, *Environ. Pollut.*, 291,
667 118249, <https://doi.org/10.1016/j.envpol.2021.118249>, 2021.

668 Liu, Y., Geng, G., Cheng, J., Liu, Y., Xiao, Q., Liu, L., Shi, Q., Tong, D., He, K., Zhang, Q.: Drivers of
669 increasing ozone during the two phases of clean air actions in China 2013–2020, *Environ. Sci. Technol.*,
670 57, 8954-8964, <https://doi.org/10.1021/acs.est.3c00054>, 2023.

671 Liu, Y., Wang, T.: Worsening urban ozone pollution in China from 2013 to 2017 – Part 1: The complex
672 and varying roles of meteorology, *Atmos. Chem. Phys.*, 20, 6305-6321, <https://doi.org/10.5194/acp-20-6305-2020>, 2020a.

673 Liu, Y., Wang, T.: Worsening urban ozone pollution in China from 2013 to 2017 – Part 2: The effects of
674 emission changes and implications for multi-pollutant control, *Atmos. Chem. Phys.*, 20, 6323-6337,
675 <https://doi.org/10.5194/acp-20-6323-2020>, 2020b.

676 Lu, X., Zhang, L. & Shen, L.: Meteorology and climate influences on tropospheric ozone: a review of
677 natural sources, chemistry, and transport patterns. *Curr. Pollution Rep.* 5, 238 – 260,
678 <https://doi.org/10.1007/s40726-019-00118-3>, 2019.

679 Lundberg, S.M., Erion, G., Chen, H., DeGrave, A., Prutkin, J.M., Nair, B., Katz, R., Himmelfarb, J.,
680 Bansal, N., Lee, S.I.: From local explanations to global understanding with explainable AI for trees.
681 *Nat. Mach. Intell.*, 2, 56-67, <https://doi.org/10.1038/s42256-019-0138-9>, 2020.

682 Ma, X., Yin, Z.: Dipole pattern of summer ozone pollution in the east of China and its connection with
683 climate variability, *Atmos. Chem. Phys.*, 21, 16349-16361, <https://doi.org/10.5194/acp-21-16349-2021>, 2021.

684 Mallapaty, S.: China's extreme weather challenges scientists trying to study it, *Nature*, 609, 888-888,
685 <https://doi.org/10.1038/d41586-022-02954-8>, 2022.

686 Meng, Q., Zhang, Y., Zhong, S., Fang, J., Tang, L., Rao, Y., Zhou, M., Qiu, J., Xu, X., Petit, J.-E.J.A.C.,
687 Physics: Reconstructing missing surface aerosol elemental carbon data in long-term series with
688 ensemble learning, *Atmos. Chem. Phys.*, 25, 7485-7498, <https://doi.org/10.5194/acp-25-7485-2025>,
689 2025.

690 Pu, X., Wang, T.J., Huang, X., Melas, D., Zanis, P., Papanastasiou, D.K., Poupkou, A.: Enhanced surface
691 ozone during the heat wave of 2013 in Yangtze River Delta region, China, *Sci. Total Environ.*, 603-
692 604, 807-816, <https://doi.org/10.1016/j.scitotenv.2017.03.056>, 2017.

693 Qin, M., She, Y., Wang, M., Wang, H., Chang, Y., Tan, Z., An, J., Huang, J., Yuan, Z., Lu, J., Wang, Q.,
694 Liu, C., Liu, Z., Xie, X., Li, J., Liao, H., Pye, H.O.T., Huang, C., Guo, S., Hu, M., Zhang, Y., Jacob,
695 D.J., Hu, J.: Increased urban ozone in heatwaves due to temperature-induced emissions of

699 anthropogenic volatile organic compounds, *Nat. Geosci.*, 18, 50-56, <https://doi.org/10.1038/s41561-024-01608-w>, 2025.

700

701 Ren, J., Guo, F., Xie, S.: Diagnosing ozone-NO_x-VOC sensitivity and revealing causes of ozone
702 increases in China based on 2013–2021 satellite retrievals, *Atmos. Chem. Phys.*, 22, 15035-15047,
703 <https://doi.org/10.5194/acp-22-15035-2022>, 2022.

704 Shen, L., Jacob, D.J., Zhu, L., Zhang, Q., Zheng, B., Sulprizio, M.P., Li, K., De Smedt, I., González Abad,
705 G., Cao, H., Fu, T.-M., Liao, H.: The 2005–2016 trends of formaldehyde columns over China observed
706 by satellites: increasing anthropogenic emissions of volatile organic compounds and decreasing
707 agricultural fire emissions, *Geophys. Res. Lett.*, 46, 4468-
708 4475, <https://doi.org/10.1029/2019GL082172>, 2019.

709 Shen, L., Mickley, L.J., Murray, L.T.: Influence of 2000–2050 climate change on particulate matter in
710 the United States: results from a new statistical model, *Atmos. Chem. Phys.*, 17, 4355-4367,
711 <https://doi.org/10.5194/acp-17-4355-2017>, 2017.

712 Shi, X., Brasseur, G.P.: The response in air quality to the reduction of Chinese economic activities during
713 the COVID-19 outbreak, *Geophys. Res. Lett.*, 47, e2020GL088070,
714 <https://doi.org/10.1029/2020GL088070>, 2020.

715 Shi, Z., Song, C., Liu, B., Lu, G., Xu, J., Van Vu, T., Elliott, R.J.R., Li, W., Bloss, W.J., Harrison, R.M.:
716 Abrupt but smaller than expected changes in surface air quality attributable to COVID-19 lockdowns,
717 *Sci. Adv.*, 7, eabd6696, <https://doi.org/10.1126/sciadv.abd6696>, 2021.

718 Tao, C., Zhang, Y., Zhang, X., Guan, X., Peng, Y., Wang, G., Zhang, Q., Ren, Y., Zhao, X., Zhao, R.,
719 Wang, Q., Wang, W.: Discrepant global surface ozone responses to emission- and heatwave-induced
720 regime shifts, *Environ. Sci. Technol.*, 58, 22288-22297, <https://doi.org/10.1021/acs.est.4c08422>, 2024.

721 Vu, T.V., Shi, Z., Cheng, J., Zhang, Q., He, K., Wang, S., Harrison, R.M.: Assessing the impact of clean
722 air action on air quality trends in Beijing using a machine learning technique, *Atmos. Chem. Phys.*, 19,
723 11303-11314, <https://doi.org/10.5194/acp-19-11303-2019>, 2019.

724 Wang, J., Wang, P., Tian, C., Gao, M., Cheng, T., Mei, W.: Consecutive Northward super typhoons
725 induced extreme ozone pollution events in Eastern China, *npj Clim. Atmos. Sci.*, 7,
726 244, <https://doi.org/10.1038/s41612-024-00786-z>, 2024a.

727 Wang, L., Chen, B., Ouyang, J., Mu, Y., Zhen, L., Yang, L., Xu, W., Tang, L.: Causal-inference machine
728 learning reveals the drivers of China's 2022 ozone rebound, *Environ. Sci. Ecotech.*, 24, 100524,
729 <https://doi.org/10.1016/j.ese.2025.100524>, 2025.

730 Wang, M., Chen, X., Jiang, Z., He, T.-L., Jones, D., Liu, J., Shen, Y.: Meteorological and anthropogenic
731 drivers of surface ozone change in the North China Plain in 2015–2021, *Sci. Total Environ.*, 906,
732 167763, <https://doi.org/10.1016/j.scitotenv.2023.167763>, 2024b.

733 Wang, N., Huang, X., Xu, J., Wang, T., Tan, Z.-m., Ding, A.: Typhoon-boosted biogenic emission
734 aggravates cross-regional ozone pollution in China, *Sci. Adv.*, 8, eabl6166,
735 <https://doi.org/10.1126/sciadv.abl6166>, 2022b.

736 Wang, R., Yang, Y., Xing, X., Wang, L., Chen, J., Tang, X., Cao, J., Morawska, L., Balkanski, Y.,
737 Hauglustaine, D., Ciais, P., Ma, J.: Stringent emission controls are needed to reach clean air targets for
738 cities in China under a warming climate, *Environ. Sci. Technol.*, 56, 11199-11211,
739 <https://doi.org/10.1021/acs.est.1c08403>, 2022c.

740 Wang, T., Xue, L., Brimblecombe, P., Lam, Y.F., Li, L., Zhang, L.: Ozone pollution in China: A review
741 of concentrations, meteorological influences, chemical precursors, and effects, *Sci. Total Environ.*,
742 575, 1582-1596, <https://doi.org/10.1016/j.scitotenv.2016.10.081>, 2017.

743 Wang, Y., Zhao, Y., Liu, Y., Jiang, Y., Zheng, B., Xing, J., Liu, Y., Wang, S., Nielsen, C.P.: Sustained
744 emission reductions have restrained the ozone pollution over China, *Nat. Geosci.*, 16, 967-974,
745 <https://doi.org/10.1038/s41561-023-01284-2>, 2023a.

746 Wang, Z.Q., Luo, H.L., Yang, S.: Different mechanisms for the extremely hot central-eastern China in
747 July-August 2022 from a Eurasian large-scale circulation perspective, *Environ. Res. Lett.*,
748 18,<https://doi.org/10.1088/1748-9326/acb3e5>, 2023b.

749 Weng, X., Forster, G.L., Nowack, P.: A machine learning approach to quantify meteorological drivers of
750 ozone pollution in China from 2015 to 2019, *Atmos. Chem. Phys.*, 22, 8385-8402,
751 <https://doi.org/10.5194/acp-22-8385-2022>, 2022.

752 World Health Organization (2021), WHO global air quality guidelines. Particulate matter (PM2.5 and
753 PM10), ozone, nitrogen dioxide, sulfur dioxide and carbon monoxide. ISBN 978-92-4-003422-8

754 Wu, K., Wang, Y., Qiao, Y., Liu, Y., Wang, S., Yang, X., Wang, H., Lu, Y., Zhang, X., Lei, Y.: Drivers of
755 2013–2020 ozone trends in the Sichuan Basin, China: Impacts of meteorology and precursor emission
756 changes, *Environ. Pollut.*, 300, 118914, <https://doi.org/10.1016/j.envpol.2022.118914>, 2022.

757 Xue, L., Ding, A., Cooper, O., Huang, X., Wang, W., Zhou, D., Wu, Z., McClure-Begley, A.,
758 Petropavlovskikh, I., Andreae, M.O., Fu, C.: ENSO and Southeast Asian biomass burning modulate
759 subtropical trans-Pacific ozone transport, *Natl. Sci. Rev.*, 8, <https://doi.org/10.1093/nsr/nwaa132>, 2020.

760 Yang, L., Luo, H., Yuan, Z., Zheng, J., Huang, Z., Li, C., Lin, X., Louie, P.K.K., Chen, D., Bian, Y.:
761 Quantitative impacts of meteorology and precursor emission changes on the long-term trend of
762 ambient ozone over the Pearl River Delta, China, and implications for ozone control strategy, *Atmos.*
763 *Chem. Phys.*, 19, 12901-12916, <https://doi.org/10.5194/acp-19-12901-2019>, 2019.

764 Yang, Y., Zhou, Y., Wang, H., Li, M., Li, H., Wang, P., Yue, X., Li, K., Zhu, J., Liao, H.: Meteorological
765 characteristics of extreme ozone pollution events in China and their future predictions, *Atmos. Chem.*
766 *Phys.*, 24, 1177-1191, <https://doi.org/10.5194/acp-24-1177-2024>, 2024.

767 Yao, T., Lu, S., Wang, Y., Li, X., Ye, H., Duan, Y., Fu, Q., Li, J.: Revealing the drivers of surface ozone
768 pollution by explainable machine learning and satellite observations in Hangzhou Bay, China, *J. Clean.*
769 *Prod.*, 440, 140938, <https://doi.org/10.1016/j.jclepro.2024.140938>, 2024.

770 Ye, X., Zhang, L., Wang, X., Lu, X., Jiang, Z., Lu, N., Li, D., Xu, J.: Spatial and temporal variations of
771 surface background ozone in China analyzed with the grid-stretching capability of GEOS-Chem High
772 Performance, *Sci. Total Environ.*, 914, 169909, <https://doi.org/10.1016/j.scitotenv.2024.169909>, 2024.

773 Yin, Y., Han, C., Yang, G., Huang, Y., Liu, M., Wang, X.: Changes in the summer extreme precipitation
774 in the Jianghuai plum rain area and their relationship with the intensity anomalies of the south Asian
775 high, *Atmos. Res.*, 236, 104793, <https://doi.org/10.1016/j.atmosres.2019.104793>, 2020.

776 Zhai, S., Jacob, D.J., Wang, X., Shen, L., Li, K., Zhang, Y., Gui, K., Zhao, T., Liao, H.: Fine particulate
777 matter (PM_{2.5}) trends in China, 2013–2018: separating contributions from anthropogenic emissions
778 and meteorology, *Atmos. Chem. Phys.*, 19, 11031-11041, <https://doi.org/10.5194/acp-19-11031-2019>,
779 2019.

780 Zhang, D.Q., Chen, L.J., Yuan, Y., Zuo, J.Q., Ke, Z.J.: Why was the heat wave in the Yangtze River valley
781 abnormally intensified in late summer 2022? *Environ. Res. Lett.*, 18, <https://doi.org/10.1088/1748-9326/acba30>, 2023.

783 Zhang, Q., Zheng, Y., Tong, D., Shao, M., Wang, S., Zhang, Y., Xu, X., Wang, J., He, H., Liu, W., Ding,
784 Y., Lei, Y., Li, J., Wang, Z., Zhang, X., Wang, Y., Cheng, J., Liu, Y., Shi, Q., Yan, L., Geng, G., Hong,
785 C., Li, M., Liu, F., Zheng, B., Cao, J., Ding, A., Gao, J., Fu, Q., Huo, J., Liu, B., Liu, Z., Yang, F., He,
786 K., Hao, J.: Drivers of improved PM_{2.5} air quality in China from 2013 to 2017, *Proc. Natl. Acad. Sci.*

787 USA, 116, 24463-24469, <https://doi.org/10.1073/pnas.1907956116>, 2019.

788 Zhang, Y., Li, N., Tang, K., Wang, M., Li, H., Li, K., Zheng, B., Zhang, Q., Gao, M., Fang, J.J.S.A.:
789 Widespread surface ozone reduction triggered by dust storm disturbance on ozone production and
790 destruction chemistry. *Sci. Adv.*, 11, eadr4297, <https://doi.org/10.1126/sciadv.adr4297>, 2025.

791 Zheng, B., Tong, D., Li, M., Liu, F., Hong, C., Geng, G., Li, H., Li, X., Peng, L., Qi, J., Yan, L., Zhang,
792 Y., Zhao, H., Zheng, Y., He, K., Zhang, Q.: Trends in China's anthropogenic emissions since 2010 as
793 the consequence of clean air actions, *Atmos. Chem. Phys.*, 18, 14095-
794 14111, <https://doi.org/10.5194/acp-18-14095-2018>, 2018.

795 Zheng, B., Zhang, Q., Geng, G., Chen, C., Shi, Q., Cui, M., Lei, Y., He, K.: Changes in China's
796 anthropogenic emissions and air quality during the COVID-19 pandemic in 2020, *Earth Syst. Sci. Data*,
797 13, 2895-2907, <https://doi.org/10.5194/essd-13-2895-2021>, 2021.

798 Zheng, H., Kong, S., Zhai, S., Sun, X., Cheng, Y., Yao, L., Song, C., Zheng, Z., Shi, Z., Harrison, R.M.:
799 An intercomparison of weather normalization of PM_{2.5} concentration using traditional statistical
800 methods, machine learning, and chemistry transport models, *npj Clim. Atmos. Sci.*, 6, 214,
801 <https://doi.org/10.1038/s41612-023-00536-7>, 2023.

802